

# A Mean-Field Approach to Simulating the Merging of Collisionless Stellar Systems Using a Particle-Based Method

SHUNSUKE HOZUMI,<sup>1</sup> MASAKI IWASAWA,<sup>2</sup> AND KEIGO NITADORI<sup>2</sup>

<sup>1</sup>*Faculty of Education, Shiga University, 2-5-1 Hiratsu, Otsu, Shiga 520-0862, Japan*

<sup>2</sup>*RIKEN Center for Computational Science, 7-1-26 Minatojima-minami-machi, Chuo-ku, Kobe, Hyogo 650-0047, Japan*

(Received December 21, 2018; Accepted March 6, 2019)

## ABSTRACT

We present a mean-field approach to simulating merging processes of two spherical collisionless stellar systems. This approach is realized with a self-consistent field (SCF) method in which the full spatial dependence of the density and potential of a system is expanded in a set of basis functions for solving Poisson’s equation. In order to apply this SCF method to a merging situation where two systems are moving in space, we assign the expansion center to the center of mass of each system, the position of which is followed by a mass-less particle placed at that position initially. Merging simulations over a wide range of impact parameters are performed using both an SCF code developed here and a tree code. The results of each simulation produced by the two codes show excellent agreement in the evolving morphology of the merging systems and in the density and velocity dispersion profiles of the merged systems. However, comparing the results generated by the tree code to those obtained with the softening-free SCF code, we have found that in large impact parameter cases, a softening length of the Plummer type introduced in the tree code has an effect of advancing the orbital phase of the two systems in the merging process at late times. We demonstrate that the faster orbital phase originates from the larger convergence length to the pure Newtonian force. Other application problems suitable to the current SCF code are also discussed.

*Keywords:* galaxies: evolution — galaxies: kinematics and dynamics — methods: numerical

## 1. INTRODUCTION

$N$ -body simulation is an indispensable method for studying astronomical objects whose constituents interact gravitationally with one another. In order to reveal detailed structures of a target object which is modeled with  $N$  particles, we need to invest in it as many particles as possible. However, extremely large  $N$ -body simulations are prohibitively time-consuming because the number of force calculation per time step increases explosively as in  $\mathcal{O}(N^2)$  with increasing  $N$ , if the force exerted on a given particle is calculated by summing up the mutual gravitational forces over all other particles. This disadvantage has been ameliorated by adopting, e.g., a tree algorithm (Barnes & Hut 1986) which reduces the number of force calculation to  $\mathcal{O}(N \log N)$ . Regarding this algorithm, a recently developed numerical library called FDPS has facilitated the implemen-

tation of a tree code running with a sufficiently high speed on a massively distributed-memory parallel computer (Iwasawa et al. 2016; Namekata et al. 2018), which will promote simulations with an ever-larger number of particles.

When an  $N$ -body method is applied to collisionless systems such as galaxies and clusters of galaxies, we should pay attention to the difference between a system composed of  $N$  particles and its corresponding genuine collisionless system. In a strict sense, an  $N$ -body system in which the forces among particles are calculated, in essence, using pair-wise interactions is not collisionless. This is because the term “collisionless” means that particles interact with the mean force field generated by themselves, and so, the forces do not depend on the relative coordinates of pair-wise particles. However, by terminating an  $N$ -body simulation within a period much shorter than the two-body relaxation time even in that way of pair-wise force calculation, we are allowed to regard the system as collisionless in a practical sense. On the other hand, a mean-field approach ensures the col-

collisionless nature at least formally. In reality, if a mean field is represented by a particle-based method, Poisson fluctuations induced by the finite number of particles cause collisional effects equivalent to two-body relaxation (Hernquist & Barnes 1990). Nevertheless, such an approach is still desirable for collisionless stellar systems from some points of view. For example, once the force field is given, the orbits of all particles can be calculated independently, and thereby one  $N$ -body problem is reduced to  $N$  one-body problems, as has been pointed out by Hernquist & Ostriker (1992). This approach is thus well suited to parallel computation as shown by Hernquist et al. (1995), so that extremely large- $N$  simulations will be made feasible. In addition, if the mean field is known at each time step, we can trace the orbits of particles starting from arbitrary positions in phase space, which enables us to reproduce phase space itself at a given time, as has been demonstrated by Hozumi (1997).

We can realize a mean-field approach to simulating collisionless stellar systems using expansion techniques for solving Poisson’s equation. Above all, a self-consistent field (SCF) method termed by Hernquist & Ostriker (1992), the idea of which dates back to that of Clutton-Brock (1972, 1973), is considerably useful. The essence of the SCF method consists in expanding the density and potential of a system in a set of basis functions. In this method, the expansion of the full spatial dependence makes the cpu cost proportional to particle number  $N$ . In addition, ideal load-balancing is easily achieved on a massively parallel machine owing to the perfect scalability inherent in the collisionless nature.

One of the disadvantages intrinsic to SCF methods is the limitation in the range of applicability because the expansion center is needed at every time step. By virtue of this inconvenience, SCF methods have been applied only to stellar dynamical problems in which systems of interest are isolated and fixed in space with the center of mass being immovable such as violent relaxation of stellar systems (Hozumi & Hernquist 1995; Hozumi et al. 1996), halo evolution (Weinberg & Katz 2002), and disk evolution (Hozumi & Hernquist 2005; Hozumi 2012). However, moving systems are ubiquitous in the real Universe, as gravitationally interacting events such as tidal encounter, collision and merging are commonly observed. In particular, merging is the fundamental process of hierarchical structure formation in the universe dominated by cold dark matter. Even after galaxies have fully grown up through hierarchical merging, they encounter or collide, and frequently result in merging to each other. Accordingly, many simulations have been devoted to reproducing the characteristic appearance of

those tails, bridges, and antennae which are indicative of galaxy interactions (e.g., Toomre & Toomre 1972; Lynds & Toomre 1976; Theys & Spiegel 1977; Farouki & Shapiro 1982; Wallin & Stuart 1992; Howard et al. 1993; Barnes 1998; Naab & Burkert 2003). Therefore, if SCF methods can be applied to merging systems, we will be able to understand in detail the features produced by merging processes and the properties of merged systems using the huge number of particles. As an instance, if the cusp found in the central region of a dark matter halo (Navarro et al. 1996, 1997) arises from the merging of clumps as suggested by Fukushige & Makino (1997), an SCF technique might help elucidate the origin of the power-law nature of the cusp that continues almost down to the center by assigning a tremendously large number of particles to each clump.

In conventional  $N$ -body methods, a softening length is introduced explicitly in order to avoid numerical divergences of the mutual force when two particles pass close to each other. On the other hand, an SCF method includes implicit softening for the force calculation in the sense that the force resolution is limited to a certain degree of precision because the expansion terms of the density and potential of a system are inevitably truncated at the finite numbers in a set of basis functions. However, the non-existence of an explicit scale length in interaction forces suggests that an SCF method may be able to describe the evolution of a stellar system under the pure Newtonian force law more faithfully than an explicitly softening-dependent method. In general, gravitational softening affects more severely the dynamics of so-called cold, rotation-dominated systems like galaxy disks (Miller 1971, 1974; Earn & Sellwood 1995) than that of hot systems like elliptical galaxies which are supported by velocity dispersion. In a sense, the orbital motion of two merging spherical galaxies is dynamically cold, even though each galaxy is a hot elliptical-like system. Consequently, the softened gravity might influence a merging process. In fact, we will uncover the effects of a softening length on the orbital phase of two merging systems.

In this paper, we present merging simulations of two spherical collisionless stellar systems on the basis of a mean-field approach which is realized using an SCF code developed here. In Section 2, models and initial settings employed are described. In Section 3, we explain how an SCF method is applied to merging simulations, along with the details of tree code simulations which are used not only for comparison but for making clear the effects of a softening length. Results are shown in Section 4. We discuss the effects of a softening length, computa-

tion time, and application problems of the SCF code for merging simulations. Conclusions are given in Section 5.

## 2. MODELS

We use two identical spherical King models (King 1966) for merging simulations. The distribution function (DF) of a King model is expressed by

$$f(\mathcal{E}) = \begin{cases} \frac{\rho_1}{(2\pi\sigma^2)^{3/2}}(e^{\mathcal{E}/\sigma^2} - 1) & (\mathcal{E} > 0), \\ 0 & (\mathcal{E} \leq 0), \end{cases} \quad (1)$$

where  $\rho_1$  and  $\sigma$  are some constants which have the dimensions of density and velocity dispersion, respectively. In Equation (1),  $\mathcal{E}$  is the relative energy defined by

$$\mathcal{E} = \Psi(r) - \frac{1}{2}(v_x^2 + v_y^2 + v_z^2), \quad (2)$$

where  $\Psi$  is the relative potential,  $r$  is the radial distance from the center, and  $v_x, v_y$ , and  $v_z$  are the three Cartesian components of the velocity vector. The potential of the system,  $\Phi$ , is related to  $\Psi$  as

$$\Phi(r) = -\Psi(r) - \frac{GM}{r_t}, \quad (3)$$

where  $G$  is the gravitational constant,  $M$  is the total mass, and  $r_t$  is the tidal radius that makes the system finite with  $\Psi(r_t) = 0$ .

We use the dimensionless central potential  $W_0 = 3$ , where  $W_0$  is defined by  $W_0 = \Psi(0)/\sigma^2$ , eliminating the arbitrariness of the DF shown in Equation (1). In this case, we have  $r_t = 4.70 r_0$  with  $r_0$  being the core radius such that

$$r_0 = \sqrt{\frac{9\sigma^2}{4\pi G\rho_0}}, \quad (4)$$

where  $\rho_0$  is the central density.

The King model is realized with  $N = 10,000,584$  particles of equal mass. A dimensionless system of units is chosen such that  $G = 1$ ,  $M = 1$ , and  $r_0 = 1$ .

We set the  $xy$ -plane to be the orbital plane of the two systems. At the beginning, each system is put on

**Table 1.** Initial Cartesian coordinates of the centers of the two systems.

Name	System 1	System 2
Case 0	(−5, 0, 0)	(5, 0, 0)
Case 1	(−5, −1, 0)	(5, 1, 0)
Case 2	(−5, −2, 0)	(5, 2, 0)
Case 3	(−5, −3, 0)	(5, 3, 0)
Case 4	(−5, −4, 0)	(5, 4, 0)
Case 5	(−5, −5, 0)	(5, 5, 0)

either side of the  $y$ -axis. The system placed in the region with  $x < 0$  and that in the region with  $x > 0$  are called System 1 and System 2, respectively. We study 6 cases listed in Table 1. The initial velocity components,  $(v_{0,x}, v_{0,y}, v_{0,z})$ , of the centers of mass of System 1 and System 2 are, respectively, (0.2, 0, 0) and (−0.2, 0, 0).

## 3. METHODS

### 3.1. SCF Method

Suppose that there exists a basis set consisting of density and potential basis functions denoted by  $\rho_{nlm}(\mathbf{r})$  and  $\Phi_{nlm}(\mathbf{r})$ , respectively, where  $n$  is a discrete number in the radial direction,  $l$  and  $m$  are corresponding quantities in the angular directions, and  $\mathbf{r}$  is the position vector. Each pair of the basis functions satisfies Poisson's equation written by

$$\nabla^2 \Phi_{nlm}(\mathbf{r}) = 4\pi G \rho_{nlm}(\mathbf{r}), \quad (5)$$

and the density and potential basis functions have the bi-orthonormality represented by

$$\int \rho_{nlm}(\mathbf{r}) \Phi_{n'l'm'}(\mathbf{r}) d\mathbf{r} = \delta_{nn'} \delta_{ll'} \delta_{mm'}, \quad (6)$$

where  $\delta_{kk'}$  is the Kronecker delta defined by  $\delta_{kk'} = 0$  for  $k \neq k'$  and  $\delta_{kk'} = 1$  for  $k = k'$ . Then, Poisson's equation for an isolated self-gravitating system is solved by expanding its density and potential in that basis set with respect to its center of mass. As a consequence, we find

$$\rho(\mathbf{r}) = \sum_{n,l,m} A_{nlm}(t) \rho_{nlm}(\mathbf{r}) \quad (7)$$

and

$$\Phi(\mathbf{r}) = \sum_{n,l,m} A_{nlm}(t) \Phi_{nlm}(\mathbf{r}), \quad (8)$$

where  $A_{nlm}(t)$  are the expansion coefficients at time  $t$ .

Once a basis set is given, the potential basis functions,  $\Phi_{nlm}(\mathbf{r})$ , are operated to the underlying density distribution,  $\rho(\mathbf{r})$ , which can be expressed by Equation (7), and then,  $A_{nlm}(t)$  are obtained with the help of the bi-orthonormality between  $\rho_{nlm}(\mathbf{r})$  and  $\Phi_{nlm}(\mathbf{r})$  indicated by Equation (6) such that

$$\begin{aligned} \int \rho(\mathbf{r}) \Phi_{nlm}(\mathbf{r}) d\mathbf{r} &= \int \sum_{n',l',m'} A_{n'l'm'}(t) \rho_{n'l'm'}(\mathbf{r}) \\ &\quad \times \Phi_{nlm}(\mathbf{r}) d\mathbf{r} \\ &= \sum_{n',l',m'} A_{n'l'm'}(t) \delta_{n'n} \delta_{l'l} \delta_{m'm} \\ &= A_{nlm}(t). \end{aligned} \quad (9)$$

On the other hand, since an  $N$ -body system is a collection of discrete mass-points, we find

$$\begin{aligned} A_{nlm}(t) &= \int \rho(\mathbf{r}) \Phi_{nlm}(\mathbf{r}) d\mathbf{r} \\ &= \int \sum_k m_k \delta(\mathbf{r} - \mathbf{r}_k) \Phi_{nlm}(\mathbf{r}) d\mathbf{r} \\ &= \sum_k m_k \Phi_{nlm}(\mathbf{r}_k), \end{aligned} \quad (10)$$

where  $m_k$  is the mass of the  $k$ -th particle in the system,  $\mathbf{r}_k$  is its position vector at time  $t$ , and  $\delta(\mathbf{r})$  is Dirac's delta function.

We can therefore compute  $\Phi(\mathbf{r})$  from Equations (8) and (10). This potential then yields the acceleration,  $\mathbf{a}(\mathbf{r})$ , by differentiating Equation (8) with respect to  $\mathbf{r}$ , leading to

$$\mathbf{a}(\mathbf{r}) = - \sum_{n,l,m} A_{nlm}(t) \nabla \Phi_{nlm}(\mathbf{r}), \quad (11)$$

where  $\nabla \Phi_{nlm}(\mathbf{r})$  can be calculated analytically in advance. The system is evolved forward in time by a time step  $\Delta t$  with a suitable integration scheme using Equation (11). In this way, we can follow the evolution of the system by iterating this procedure.

In contrast with isolated systems, two interacting systems like those studied here are moving in space, which implies that the center of mass (CM) of each system is not fixed but moving with time. It thus follows that we need to locate the expansion centers of the two systems at every time step. For this purpose, when starting a simulation, we first put a mass-less particle at the CM of each system as a guide of the expansion center, and trace the position of that particle by summing over all two-body interactions of it with the self-gravitating particles. That is, the acceleration of the mass-less particle in System  $i$  ( $i = 1$  or  $2$ ),  $\mathbf{a}(\mathbf{r}_{\text{CM},i})$ , is calculated as

$$\mathbf{a}(\mathbf{r}_{\text{CM},i}) = - \sum_k \frac{G m_k (\mathbf{r}_k - \mathbf{r}_{\text{CM},i})}{|\mathbf{r}_k - \mathbf{r}_{\text{CM},i}|^3}, \quad (12)$$

where  $\mathbf{r}_{\text{CM},i}$  is the position vector of the mass-less particle in System  $i$ , and  $\mathbf{r}_k$  stands for the position vector of the  $k$ -th self-gravitating particle with the mass being  $m_k$  in the total system. Then, we calculate the self-gravity of each system by expanding the density and potential of the corresponding system around its expansion center. The acceleration of a particle in System  $i$  due to the self-gravity,  $\mathbf{a}_{i \rightarrow i}(\mathbf{r})$ , is represented by

$$\mathbf{a}_{i \rightarrow i}(\mathbf{r}) = \sum_{n,l,m} A_{nlm,i}(t) \nabla \Phi_{nlm}(\mathbf{r} - \mathbf{r}_{\text{CM},i}), \quad (13)$$

where  $A_{nlm,i}(t)$  are the expansion coefficients of System  $i$  at time  $t$  with the expansion center being  $\mathbf{r}_{\text{CM},i}$ .

Here, we assume that the same basis set is used for Systems 1 and 2, since we deal with the merging of two identical King models. Next, the interaction forces exerted on the particles in one system by those in the other system are evaluated by applying the expansion coefficients of the other system to the forces at their positions. That is, the acceleration of a particle in System  $i$  caused by the force field of System  $j$  ( $i \neq j$ ),  $\mathbf{a}_{j \rightarrow i}(\mathbf{r})$ , is given by

$$\mathbf{a}_{j \rightarrow i}(\mathbf{r}) = \sum_{n,l,m} A_{nlm,j}(t) \nabla \Phi_{nlm}(\mathbf{r} - \mathbf{r}_{\text{CM},j}), \quad (14)$$

where  $A_{nlm,j}(t)$  are the expansion coefficients of System  $j$  at time  $t$  with the expansion center being  $\mathbf{r}_{\text{CM},j}$ .

For large impact parameters, however, we have found that the calculation method based on Equation (14) bears large errors. Instead, we expand a system of interest with respect to the CM of the total system, and apply the expansion coefficients of that system to the forces suffered by the particles in the other system. Thus, instead of Equation (14), we use

$$\mathbf{a}_{j \rightarrow i}(\mathbf{r}) = \sum_{n,l,m} A_{nlm,j}^{(\text{CM})}(t) \nabla \Phi_{nlm}(\mathbf{r} - \mathbf{r}_{\text{CM}}), \quad (15)$$

where  $A_{nlm,j}^{(\text{CM})}(t)$  are the expansion coefficients calculated by expanding System  $j$  around the CM of the total system,  $\mathbf{r}_{\text{CM}}$ . In reality, the conservation of linear momentum leads to  $\mathbf{r}_{\text{CM}} = 0$ , and  $A_{nlm,j}^{(\text{CM})}(t)$  are identical to  $A_{nlm,i}^{(\text{CM})}(t)$  ( $i \neq j$ ), since the two identical King models are set up initially in a configuration symmetric about the origin. In these cases, again, we use the same basis set for the interaction forces between the two systems as that used for the self-gravity. After all, the acceleration of a particle in System  $i$ ,  $\mathbf{a}_i(\mathbf{r})$ , is calculated as

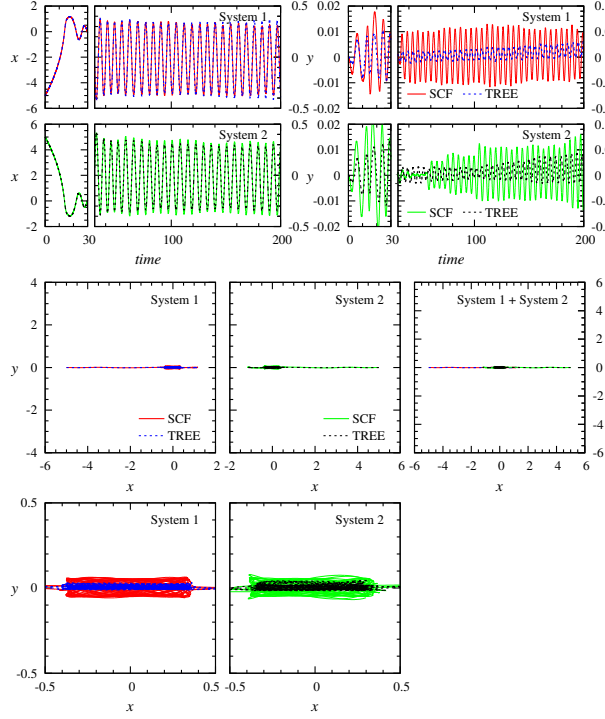
$$\mathbf{a}_i(\mathbf{r}) = \mathbf{a}_{i \rightarrow i}(\mathbf{r}) + \mathbf{a}_{j \rightarrow i}(\mathbf{r}) \quad (i \neq j). \quad (16)$$

Since the King model has a core structure, the basis functions suitable for the present study are those which are not cuspy but cored. Accordingly, we select Clutton-Brock's basis set (Clutton-Brock 1973) which is constructed on the basis of the Plummer model (Plummer 1911). The exact functional forms of the basis set employed are given in Appendix A. The scale length of the basis functions,  $a$ , is set to be  $a = 1.15$  so as to represent the density distribution of the King model with the lowest order density term,  $\rho_{000}$ , that is identical to the density of the Plummer model, as closely as possible. We do not change the value of  $a$  even in calculating the interaction forces between the two systems.

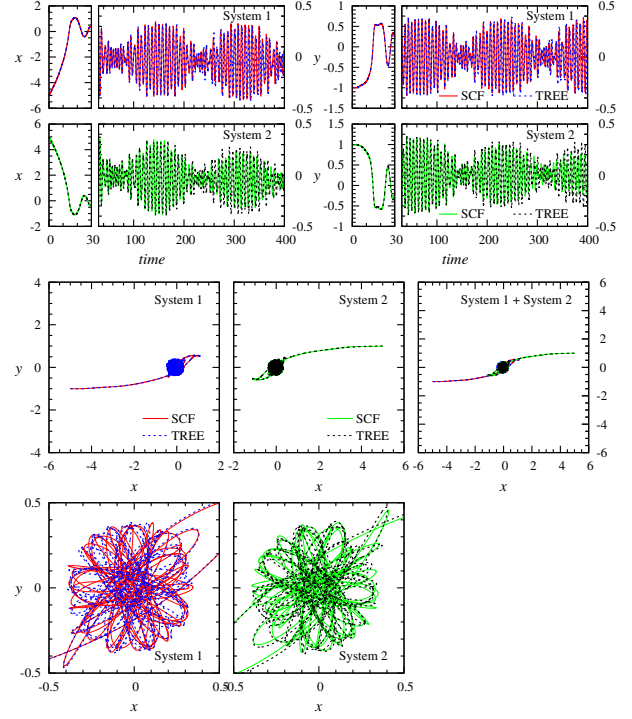
We carried out convergence tests to determine the numbers of the expansion terms. After some trials,



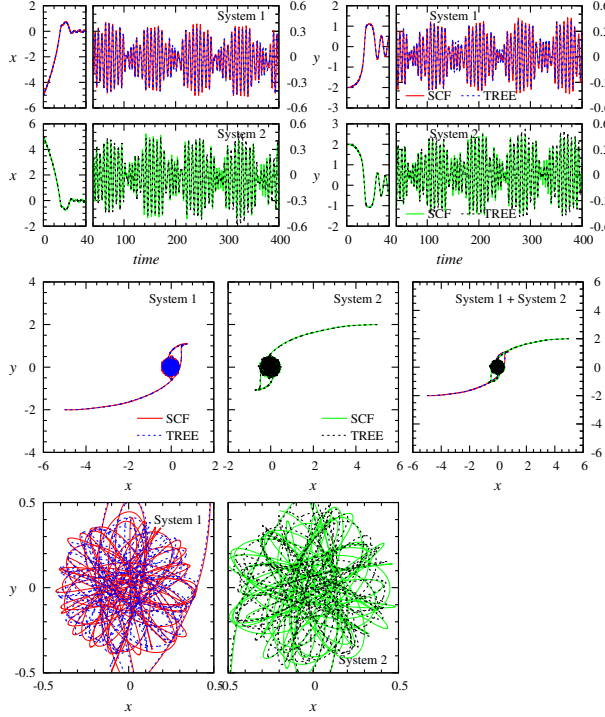
(a) Case 0



(b) Case 1



(c) Case 2



(d) Case 3

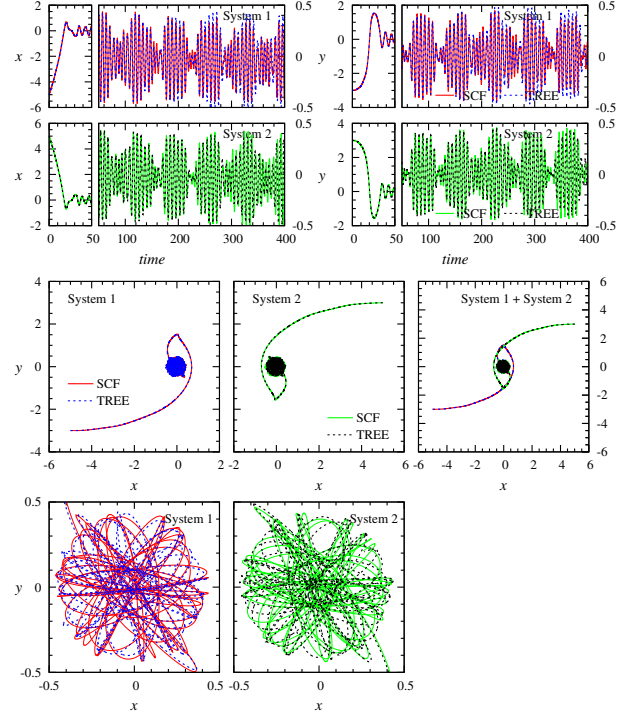
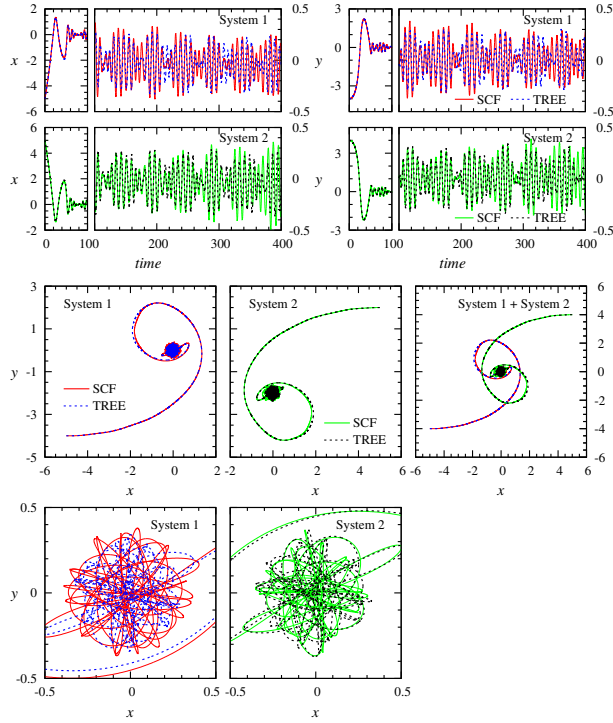


**Figure 1.** Motions of the centers of mass (CM) of Systems 1 and 2 for (a) Case 0 to (f) Case 5. In each case, in the first-row panels, the top panels show the  $x$  (left two panels) and  $y$  (right two panels) coordinates of the CM of System 1 as a function of time, while the bottom panels present those of System 2. The second-row panels display the orbit of the CM of System 1 (left panel), that of System 2 (middle panel), and that of Systems 1 and 2 (right panel). In the third-row panels, the left panel is the enlargement version of the left panel in the second row, while the right panel is that of the middle panel in the second row. The red and green solid lines represent the CM of System 1 and that of System 2, respectively, for the SCF simulation, while the blue and black dashed lines denote the CM of System 1 and that of System 2, respectively, for the tree code simulation. In the SCF simulation, the interaction forces are calculated using Equation (14).

(e) Case 4



(f) Case 5

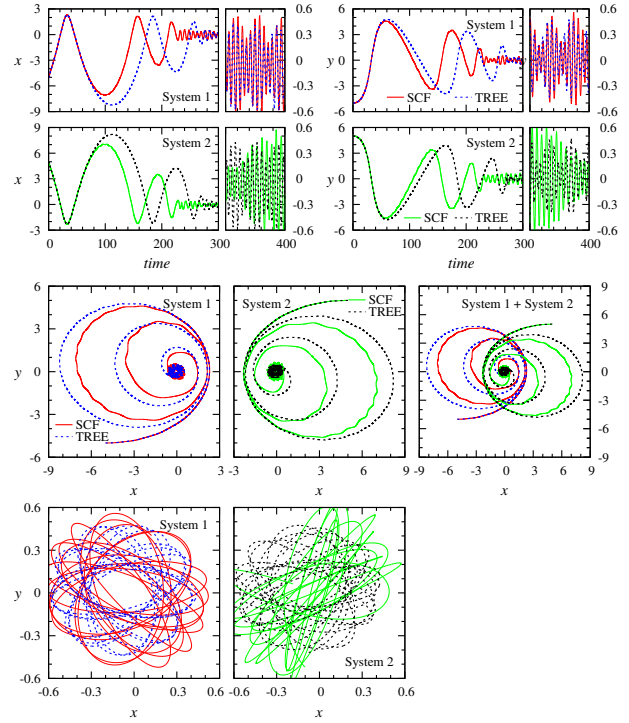
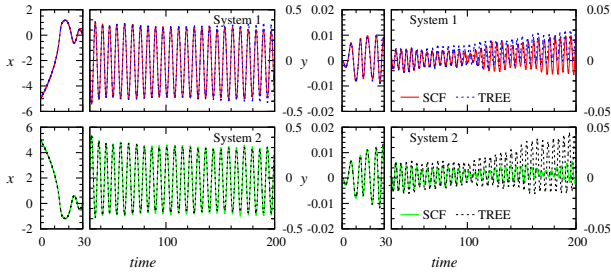


Figure 1. Continued.



**Figure 2.** Same as in the first-row panels of Figure 1 (a) for the Case 0 simulations. In the SCF simulation, the same softening length as that adopted in the tree code one was employed to calculate the orbits of the test particles placed at the centers of mass of Systems 1 and 2.

we adopt  $n_{\max} = 16$  and  $l_{\max} = m_{\max} = 10$ , where  $n_{\max}$  is the maximum number of expansion coefficients in the radial direction, and  $l_{\max}$  and  $m_{\max}$  are the maximum numbers of those in the angular directions. For the interaction forces that are calculated using the CM of the total system as the expansion center, we adopt  $n_{\max} = 28$  and  $l_{\max} = m_{\max} = 28$  with the value of  $a$  intact for the same basis set, while keeping  $n_{\max} = 16$  and  $l_{\max} = m_{\max} = 10$  for the calculations of the self-gravitating forces. Regarding the integration scheme to solve the equations of motion for the self-gravitating and mass-less particles, we employ a time-centered leapfrog

method (Press et al. 1986) with a fixed time step of  $\Delta t = 0.01$ . As a result, the energy was conserved to better than 0.0882% for all the simulations.

### 3.2. Tree Method

The same initial setups as those adopted in the SCF simulations are used for simulations with a hierarchical tree algorithm (Barnes & Hut 1986) in order to evaluate the results produced by the SCF code. In so doing, we utilize an FDPS library written in a C++ language (Iwasawa et al. 2016) which has been highly tuned for a massively distributed-memory parallel machine. In the tree approach, forces are expanded up to quadrupole order, and computed with an opening angle of 0.5, unless otherwise mentioned. We choose a gravitational softening of the Plummer type to prohibit numerical divergences when two particles pass close to each other, and set the softening length,  $\epsilon$ , to be the mean interparticle separation within the half-mass radius,  $\epsilon = 0.0074$ , again unless otherwise mentioned. In accordance with the SCF simulations, we put a mass-less particle at the center of each system to compare its orbit with that obtained using the SCF code. For the mass-less particles, the same softening length,  $\epsilon = 0.0074$ , is adopted. A time-centered leapfrog method is used with a fixed time step of  $\Delta t = 0.01$ . As a result, all the tree code simulations showed the relative energy error to be smaller than 0.0174%.

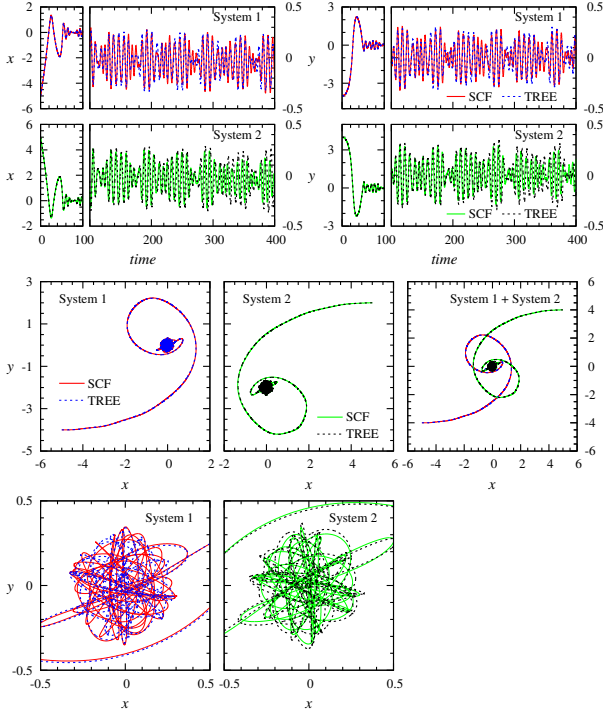


**Figure 3.** Same as in Figure 1 (e) for the Case 4 simulations, but the interaction forces are calculated on the basis of Equation (15) for the SCF simulation.

## 4. RESULTS

### 4.1. Merging Processes

In Figure 1, we compare the orbits of the centers of mass of Systems 1 and 2 for Cases 0 to 5 between the SCF and tree code simulations. The interaction forces between the two systems in these SCF simulations are calculated using Equation (14). We can see that in cases of small impact parameters for Cases 0 to 3, the orbits of the centers of mass in the SCF simulations agree quite well with those in the corresponding tree code ones. However, in Case 0 which represents a head-on collision, the fluctuating motions of the centers of mass in the  $y$ -direction are much more violent in the SCF simulation than in the tree code one, although the fluctuating amplitude is sufficiently small as compared to the size of the merged system. In order to demonstrate that this difference originates from whether the gravitational softening is introduced or not in tracing the positions of the centers of mass, we calculate them in the SCF simulation using the same softened gravity of the Plummer type with  $\varepsilon = 0.0074$  as is incorporated into the tree code, instead of using the pure Newtonian force law described by Equation (12). The results are shown in Figure 2. We find from this figure that the large fluctuating mo-

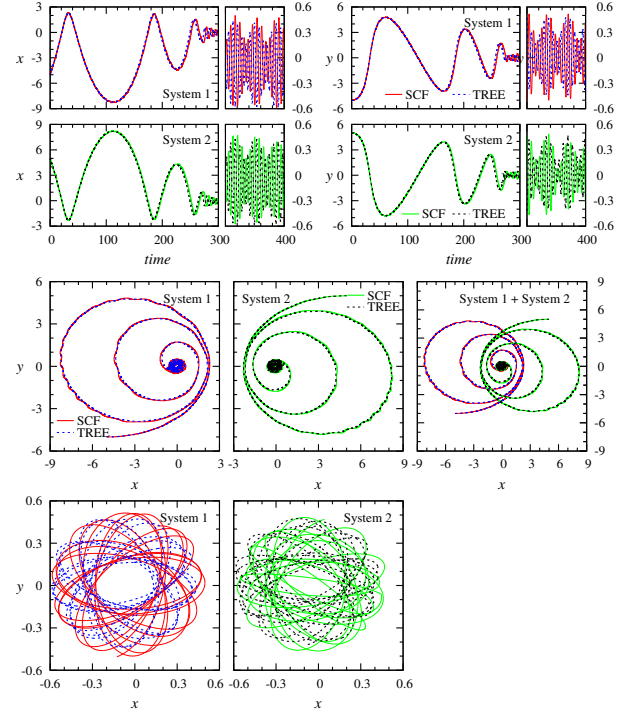


**Figure 4.** Same as in Figure 1 (f) for the Case 5 simulations, but the interaction forces are calculated on the basis of Equation (15) for the SCF simulation.

tions of the centers of mass in the  $y$ -direction are curbed in the SCF simulation to a significant degree, and that the fluctuating amplitude is rather smaller than that in the tree code simulation at late times. In addition, the  $y$ -coordinates of the centers of mass in the tree code simulation tend to deviate on average almost linearly from  $y = 0$  with time, while those in the SCF simulation fluctuate around  $y = 0$ . Accordingly, in this case, the linear momentum of the total system is better conserved for the SCF simulation than for the tree code one, although in principle, it is not strictly conserved for both the simulation methods.

Regarding large impact parameters such as Cases 4 and 5, the orbits of the centers of mass are not in good agreement between both the simulation methods at late times. We will describe the differences in detail below.

From Figure 1 (e), we can find that in Case 4, a noticeable difference exists in the orbits of the centers of mass of Systems 1 and 2 from  $t \sim 200$  to  $t \sim 240$  between the SCF and tree code simulations. If we adopt the calculation method of the interaction forces based on Equation (15) instead of that based on Equation (14), desired results are obtained as presented in Figure 3 which shows excellent agreement between the two simulation methods.



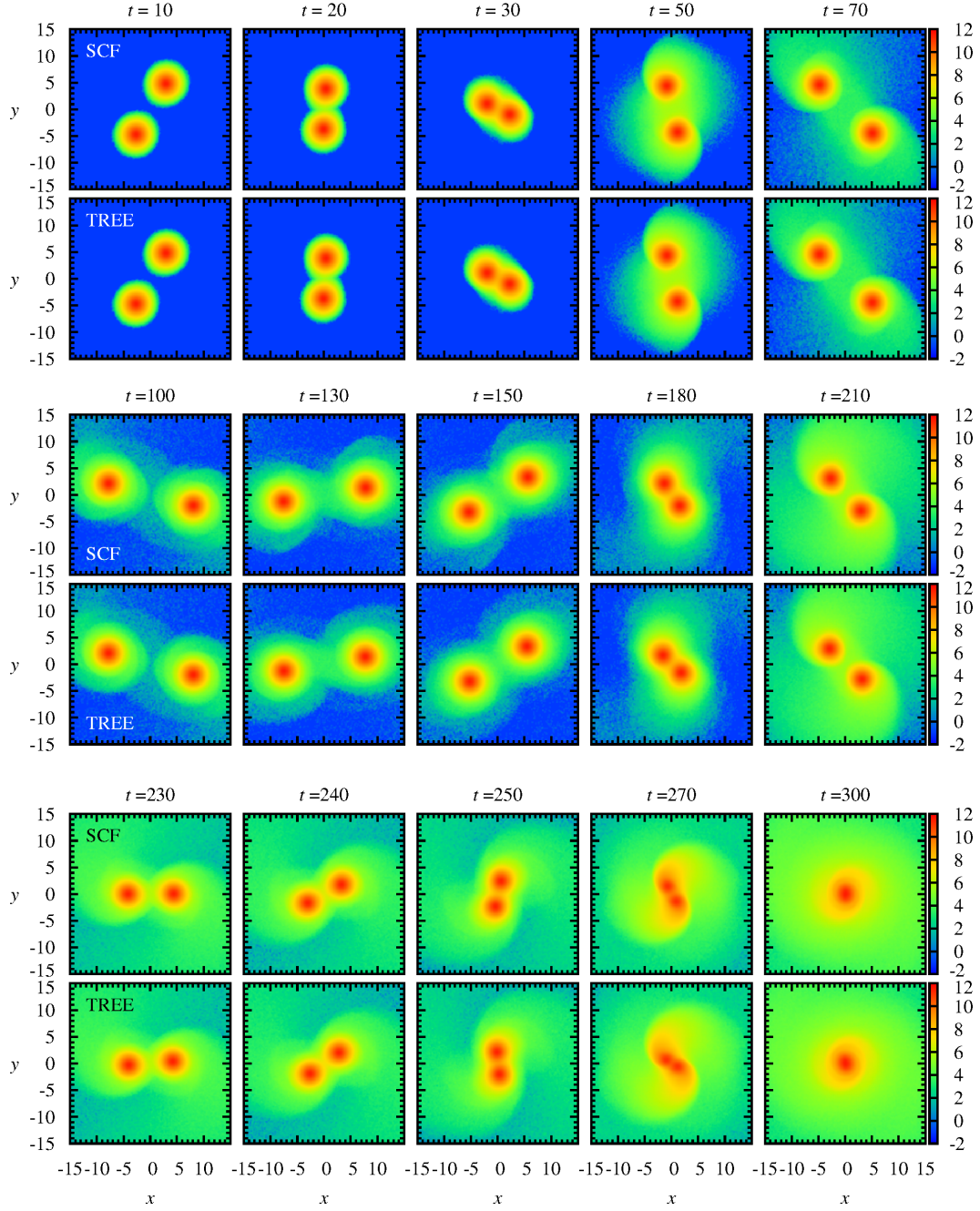


**Figure 5.** Comparison of the time evolution of the density distribution of Systems 1 and 2 in the orbital plane for the Case 5 simulations between the SCF (top panels at each time) and tree code (bottom panels at each time) simulations. The density distributions are represented on a logarithmic scale.

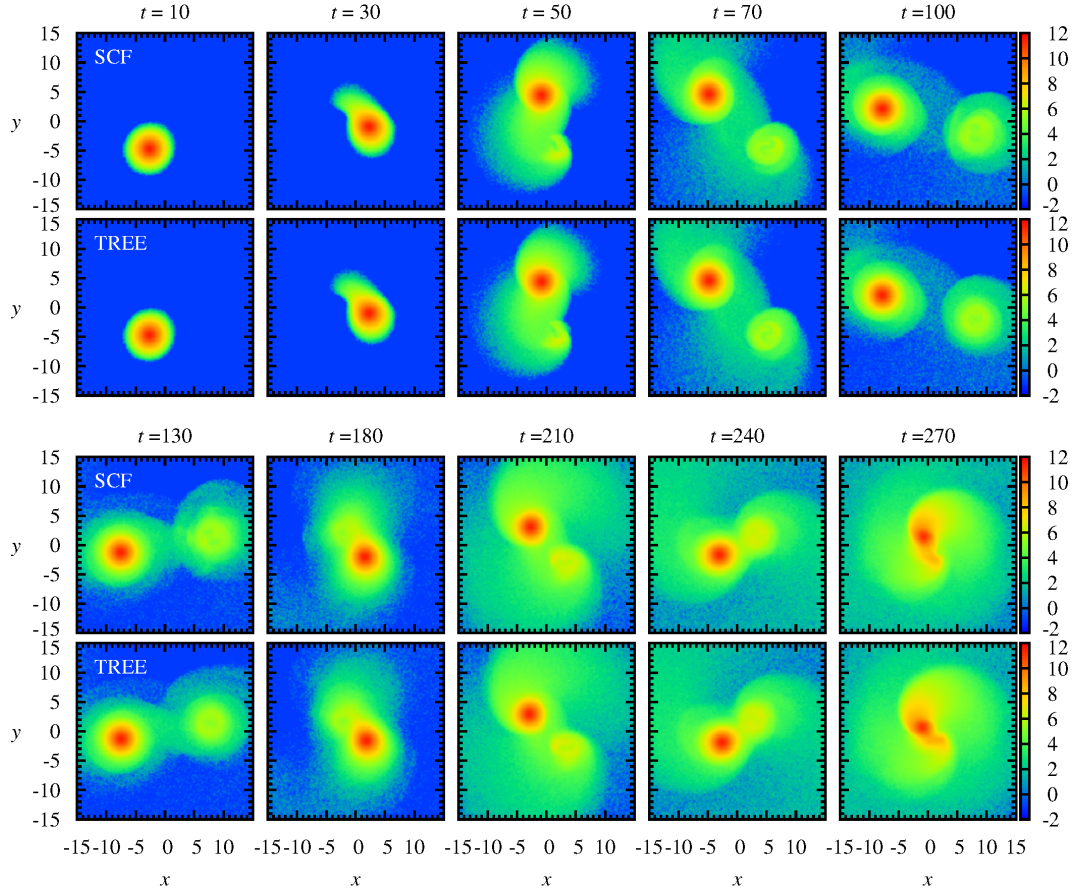


**Figure 6.** Comparison of the time evolution of the density distribution of System 1 in the orbital plane for the Case 5 simulations between the SCF (top panels at each time) and tree (bottom panels at each time) simulations. The density distributions are represented on a logarithmic scale.

Figure 1 (f) reveals that in Case 5, the difference in the orbits of the centers of mass between the two simulation methods becomes extremely large after  $t \sim 60$ . In addition, the fourth-row panels indicate that the orbit of the CM in System 2 for the SCF simulation is rather aligned at late time phases of merging, while that in System 1 draws a rosette-like feature. Taking into consideration the symmetric configuration of the two identical systems at the beginning, such a spatially non-uniform distribution of the orbit around the center of the system should not be expected. In fact, the tree code simulation does not exhibit such an alignment tendency in the orbit. As shown in Figure 4, this undesired behavior is eliminated by adopting the alternative calculation method based on Equation (15) for the interaction forces, and so, the SCF and tree code simulations agree quite well with each other.

In Figure 5, we present the time evolution of the density distributions of Systems 1 and 2 projected on the orbital plane for Case 5 using the SCF and tree codes. For the SCF simulation, the interaction forces are calculated on the basis of Equation (15). This figure demon-

strates that the density distribution in the merging two systems with the SCF method evolves quite similarly to that with the tree method. To depict in detail how the individual systems are tidally deformed in the merging process in this case, Figure 6 illustrates the time evolution of the projected density distribution of System 1 on the orbital plane for the SCF and tree code simulations. We notice that around  $t = 50$ , a small fraction of particles is stripped off the main body, subsequently falling into the central region of System 2. Figure 6 convinces us that the SCF method can describe the stripping process quite similarly to that with the tree method, even though the system is torn apart.

In Figures 5 and 6, a closer look at the evolution of the projected density distribution after  $t = 240$  for Case 5 reveals that the orbital phase of the two systems in the tree code simulation advances faster than that in the SCF simulation. We will discuss this behavior in relation to the effects of gravitational softening in the next section.

#### 4.2. Merged Systems



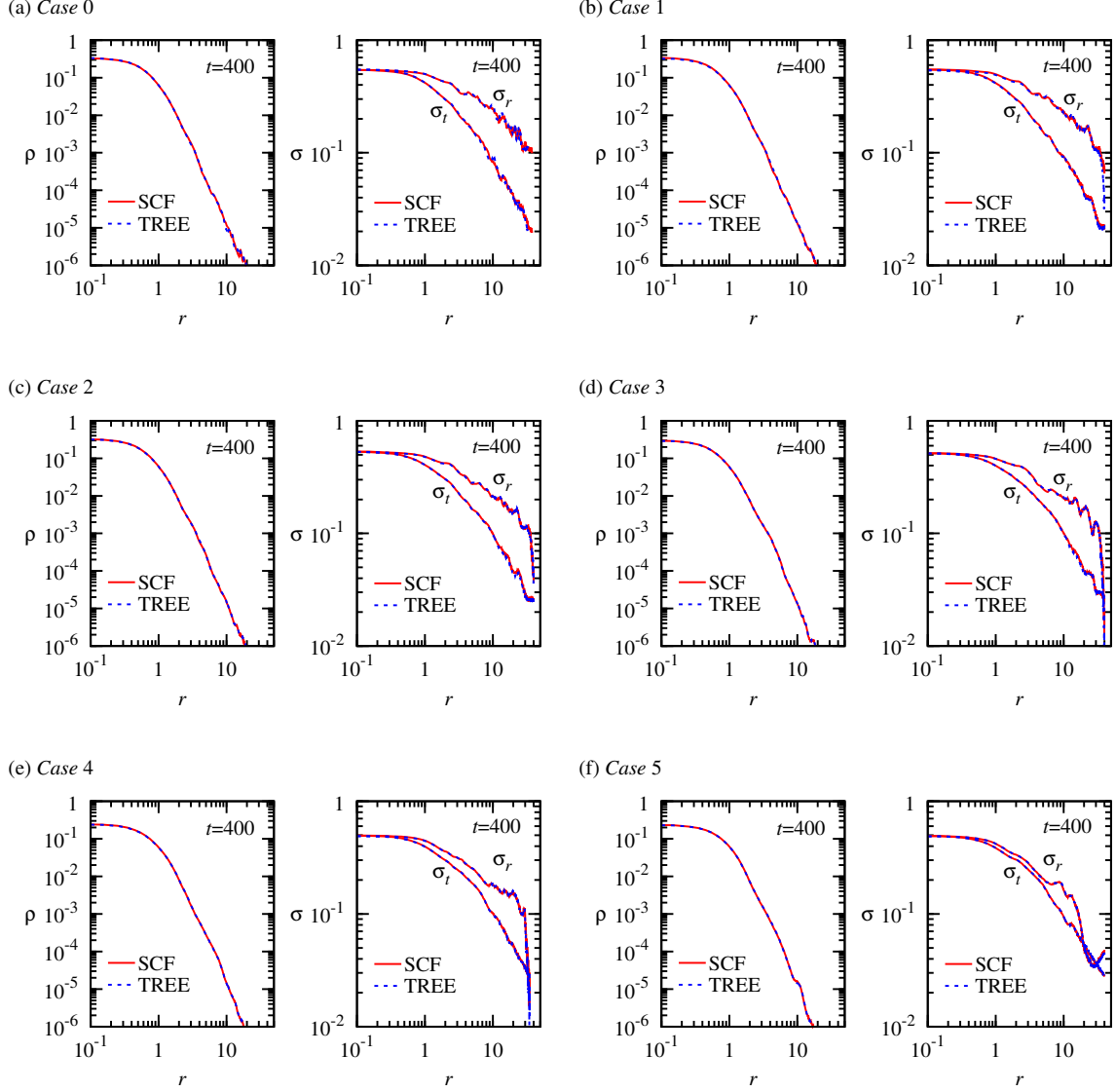


**Figure 7.** Density and velocity dispersion profiles of the merged system for (a) Case 0 to (f) Case 5 at  $t = 400$ . For each case, the left panel shows the density profile, while the right panel presents the radial,  $\sigma_r$ , and tangential,  $\sigma_t$ , velocity dispersion profiles. The red solid and blue dashed lines correspond to the SCF and tree code simulations, respectively.

We have found that the two systems in all cases result in almost completely merged states by  $t = 400$ . We have also found that the centers of mass of the two systems continue to oscillate back and forth around the CM of the total system for long periods, even though they have merged seemingly into a single system, but that the oscillation amplitude is sufficiently small as compared to the size of the merged system as found from Figure 1.

In Figure 7, we compare the spherically averaged density and radial and tangential velocity dispersion profiles of the merged systems at  $t = 400$  for Cases 0 to 5 between the SCF and tree code simulations. We find from these figures that both the simulation methods provide almost identical distributions in the density and radial and tangential velocity dispersions for the merged sys-

tem in each case, which implies that the softened gravity does not affect them at radii sufficiently larger than the softening length.

## 5. DISCUSSION

### 5.1. Effects of softening length

We first discuss the finding mentioned in Subsection 4.1 that the softening length accelerates the advancement of the orbital phase between the two systems in the large impact parameter cases. In order to confirm this effect, we carry out simulations for Case 5 with the softening length changed. Figure 8 shows how the density distribution evolves over time for each value of  $\varepsilon = 0.0074, 0.0148, 0.0222$ , and  $0.0296$ , while the opening angle of  $0.5$  is retained, together with the density

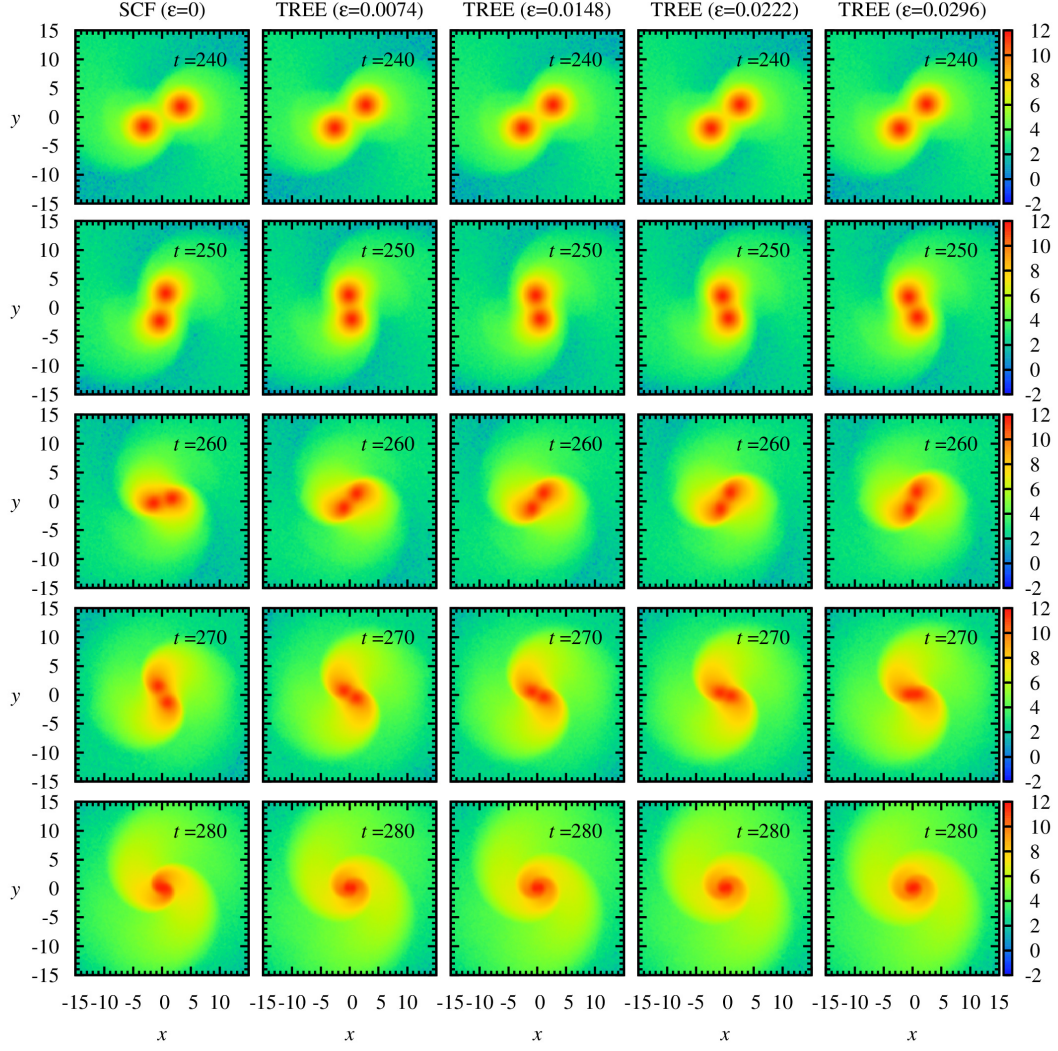


**Figure 8.** Time evolution of the density distribution of Systems 1 and 2 in the orbital plane for the Case 5 simulations. The first column shows the density distributions produced from the SCF simulation that corresponds to a zero softening length ( $\varepsilon = 0$ ). The second to fifth columns depict those from the tree code simulations with the Plummer softening lengths of  $\varepsilon = 0.0074, 0.0148, 0.0222$  and  $0.0296$ , respectively. As the softening increases, the orbital phase of the two systems advances faster. The density distributions are represented on a logarithmic scale. The snapshot time is denoted at the top right corner.

distribution produced by the SCF simulation that corresponds to  $\varepsilon = 0$ . This figure demonstrates clearly that the orbital phase advances faster as the softening length increases. In Figure 9, we quantify this change in the orbital phase with time by calculating the angle,  $\varphi$ , between the  $x$ -axis and the line that connects the centers of mass of Systems 1 and 2 in the orbital plane measured from  $t = 0$  at which  $\varphi = \pi/4$ . This figure obviously shows that the larger softening length results in the faster orbital phase.

We carried out another Case 5 simulation with an opening angle of 0.3 using  $\varepsilon = 0.0074$  (not presented here), and found that there was no practical difference in the orbital phase between the two opening angles of 0.3 and 0.5 as long as the same softening length of

$\varepsilon = 0.0074$  was used. It therefore follows that the change in the orbital phase is not caused by the low precision of the force calculation at large radii. Moreover, we reran the Case 5 simulations with  $\varepsilon = 0.0074$  and  $0.0148$  by doubling the time step ( $\Delta t = 0.02$ ) and confirmed that there were no essential changes in the orbital phase evolution between the results with  $\Delta t = 0.01$  and those with  $\Delta t = 0.02$  (also not presented here). It is thus unlikely that the adopted time step is the cause of the orbital phase shift.

In order to investigate the origin of the change in the orbital phase, we carry out Case 5 simulations using spline softening in which the force law shifts to the pure Newtonian one when the interparticle distance exceeds twice as large as the softening length (Hernquist & Katz

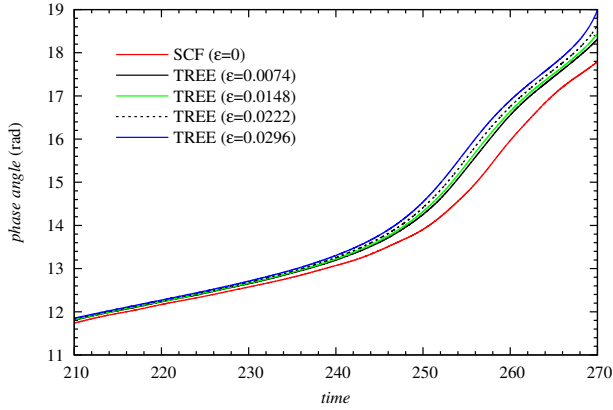


**Figure 9.** Time evolution of the phase angle for the Case 5 simulations. The phase angle is defined by the angle between the  $x$ -axis and the line connecting to the two centers of mass of Systems 1 and 2. The red solid line shows the phase angle produced from the SCF simulation, while the black solid, green solid, black dotted, and blue solid lines stand for that from the tree code simulations with the Plummer softening lengths of  $\varepsilon = 0.0074, 0.0148, 0.0222$ , and  $0.0296$ , respectively.

1989). Results are summarized in Figure 10 where the comparisons between the Plummer and spline softening are made for  $\varepsilon = 0.0074$  and  $0.0296$ . In either case of  $\varepsilon$ , the spline softening delays the orbital phase as compared to the corresponding Plummer softening. In fact, Figure 11 shows that the orbital phase for the Plummer softening advances faster than that for the spline softening if the same softening length is used. We thus infer that the advancement of the orbital phase depends on the extent of the deviation from the pure Newtonian force. Although the spline softening confines the extent of the softened force to a certain distance, it still accelerates the orbital phase faster than that in the SCF simulation.

In Figure 12, we show how the conserved quantity of the  $z$ -component of the total angular momentum,  $L_z$ , changes with time for the Case 5 tree code simulations using the Plummer softening, together with  $L_z$  for the corresponding SCF simulation. We can see that the value of  $L_z$  begins to increase rapidly at  $t \sim 210$  and remains large until  $t \sim 260$ , regardless of the softening lengths. Furthermore, the value of  $L_z$  becomes larger as the softening length increases for the period between  $t \sim 210$  and  $t \sim 260$ . Since the orbital angular momentum could contribute to the total angular momentum to a considerable degree in this case, the increase in  $L_z$  would lead to a faster orbital motion, particularly at the times after  $t \sim 240$  when the distance between the centers of mass of the two systems becomes smaller and smaller. From these circumstances, we could infer

that the orbital phase advances faster as the softening length becomes larger for that period. Figure 13 shows the time change in  $L_z$  for the Plummer and spline softening lengths of  $\varepsilon = 0.0074$  and  $0.0296$ . This figure indicates that the time change in  $L_z$  for the spline softening lengths of  $\varepsilon = 0.0074$  and  $0.0296$  is similar to that with the Plummer softening length of  $\varepsilon = 0.0074$ . Consequently, we could understand that the time evolution of the orbital phase angle for the spline softening lengths of  $\varepsilon = 0.0074$  and  $0.0296$  behaves similarly to that with the Plummer softening length of  $\varepsilon = 0.0074$ , as shown in Figure 9. However, since the increase in  $L_z$  is at most on a level of 0.02%, it is necessary to examine further whether such a slight increase can justify this reasoning. On the other hand,  $L_z$  is well-conserved in the SCF simulation, as is presented in Figures 12 and 13. This fact suggests that the SCF simulation could describe the true evolution of the merging process in this case more precisely than the tree code simulations. In fact, concerning the orbital phase, the SCF simulation appears to correspond to a limiting case of  $\varepsilon = 0$  when the softening length is decreased from  $\varepsilon = 0.0296$  to  $\varepsilon = 0.0074$  in the tree code simulations.

In order to reveal how faithfully the SCF simulations shown here can follow the true evolution, the most desirable approach may be a comparison of the simulations with the SCF code to those with a six-dimensional phase-space code developed by Yoshikawa et al. (2013), which has been touched up by Tanaka et al. (2017), or with that based on a moving adaptive simplicial tessellation method devised by Sousbie & Colombi (2016), since no gravitational softening is included in these codes. In fact, Yoshikawa et al. (2013) have presented a sample simulation of merging two identical King spheres. This implies that the comparison mentioned above is feasible.

## 5.2. Computation time

The SCF code used here has the perfect scalability (Hernquist et al. 1995), so that ideal load-balancing is easily realized on a massively parallel computer. As a consequence, on such a machine, the cpu time of an SCF simulation is proportional to  $N_{\text{core}}(n_{\text{max}}+1)(l_{\text{max}}+1)(m_{\text{max}}+1)$ , where  $N_{\text{core}}$  is the number of particles per cpu core. On the other hand, the perfect scalability cannot be realized for tree algorithms. Furthermore, in the tree code used for the current study on which the FDPS library developed by Iwasawa et al. (2016) has been implemented, an exchange of particles between computing nodes is executed for efficient load-balancing as an additional computation cost. Consequently, when 648 cpu cores are operated on a Cray XC30 system, the cpu times for the SCF simulations are  $\sim 3.2 \times 10^{-4}$  sec per step



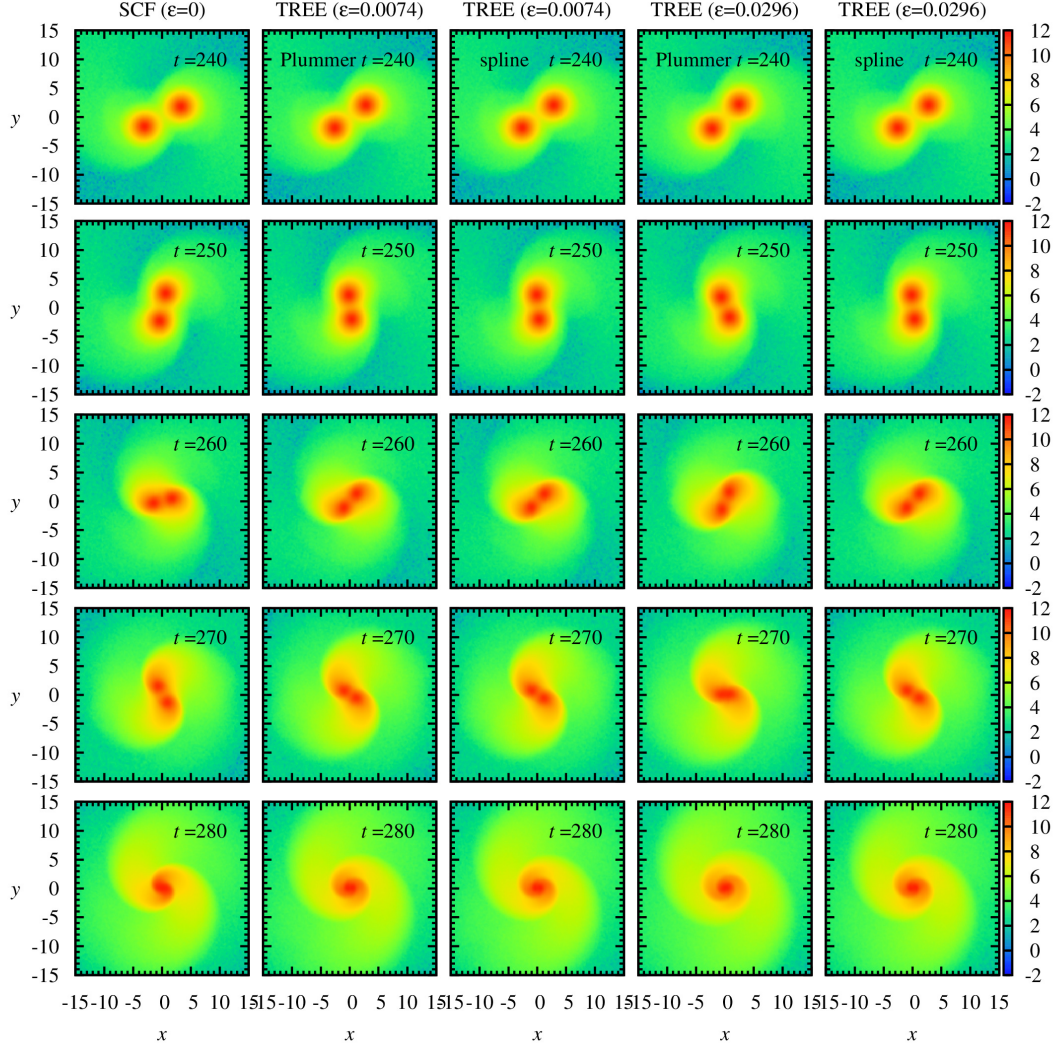


**Figure 10.** Time evolution of the density distribution of Systems 1 and 2 in the orbital plane for the Case 5 simulations. The first column shows the density distributions produced from the softening-free ( $\varepsilon = 0$ ) SCF simulation. The second and third columns exhibit those from the tree code simulations using the Plummer and spline softening lengths of  $\varepsilon = 0.0074$ , respectively, while the fourth and fifth columns depict those using the Plummer and spline softening lengths of  $\varepsilon = 0.0296$ , respectively. The density distributions are represented on a logarithmic scale. The snapshot time is denoted at the top right corner of each panel.

per core when Equation (14) is adopted, and they are  $\sim 2.5 \times 10^{-3}$  sec per step per core when Equation (15) is employed, while those for the tree code simulations are  $\sim 4.8 \times 10^{-3}$  sec per step per core. Thus, we can see that the SCF code is more than an order of magnitude faster than the tree code, when the interaction forces between the two systems are based on Equation (14), and that the former is at least twice as fast as the latter, even though the interaction forces are calculated according to Equation (15).

As Meiron et al. (2014) have implemented an SCF code for simulating isolated stellar systems on a machine carrying a GPGPU which deals with parallel computation, the present SCF code can also be adjusted to such a machine without any difficulty. It will there-

fore make feasible merging simulations with a sufficiently large number of particles on a GPGPU system within a relatively small amount of computation time.

### 5.3. Applications of the SCF code for merging

Since an SCF method is literally a field method, we can obtain a force field at each time step as an SCF simulation proceeds with time. In addition, the force field is represented by the expansion coefficients,  $A_{nlm}$ , so that even though  $A_{nlm}$  are saved at each time step, the data size is extremely small as compared to that when snapshots are saved at each time step. This means that the orbit of an arbitrary particle in phase space can be traced once an SCF simulation has been completed, because the acceleration at an arbitrary position can be

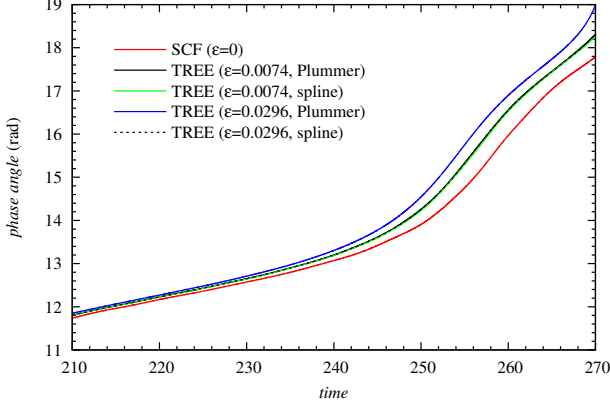


**Figure 11.** Time evolution of the phase angle for the Case 5 simulations with the tree method using the Plummer and spline softening lengths, along with the softening-free SCF method. The red line shows the phase angle produced from the SCF simulation. The black and green solid lines depict the phase angle with the Plummer and spline softening lengths of 0.0074, respectively, while the blue solid and black dotted lines exhibit that with the Plummer and spline softening lengths of 0.0296, respectively.

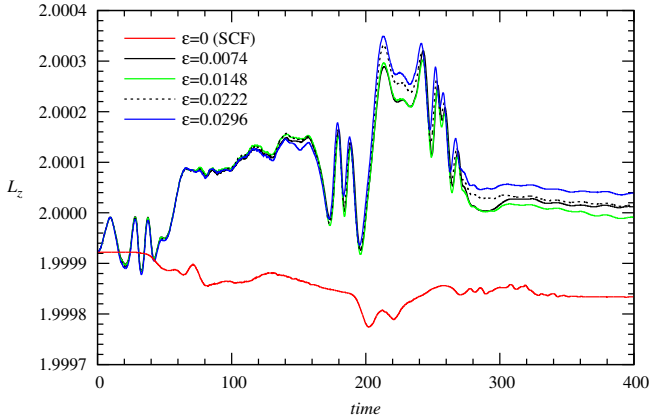


**Figure 12.** Time change in the  $z$ -component of the total angular momentum,  $L_z$ , for the Case 5 simulations with the tree method using the Plummer softening, along with the softening-free SCF method. The black solid, green solid, black dotted, and blue solid lines show  $L_z$  obtained with the softening lengths of  $\varepsilon = 0.0074, 0.0148, 0.0222$ , and  $0.0296$ , respectively, while the red line displays  $L_z$  generated by the SCF simulation.

calculated at each time step from  $A_{nlm}(t)$  as indicated by Equation (11). Therefore, phase space at a specified time can be reproduced by tracing the orbits of necessary particles at time  $t$  backward to  $t = 0$  on the basis of Liouville's theorem, as has been demonstrated by Hozumi (1997). In particular, if we analyze the structures in phase space reproduced from a merging simulation, traces of the merging process that the Milky Way experienced in the past might be found out by compar-

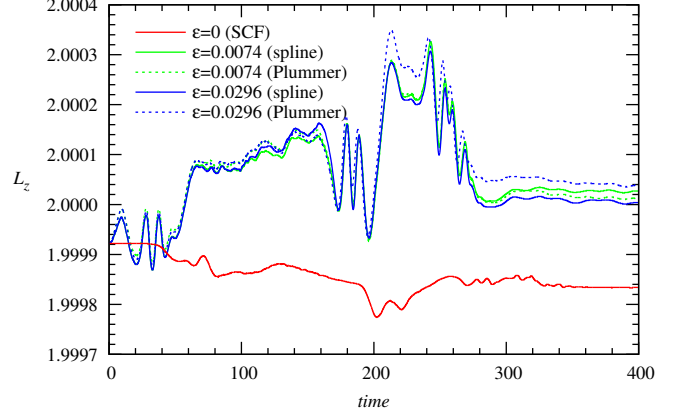


**Figure 13.** Time change in the  $z$ -component of the total angular momentum,  $L_z$ , for the Case 5 simulations with the tree method between the spline (solid lines) and Plummer (dotted lines) softening, along with the softening-free SCF method. The green and blue lines show  $L_z$  obtained with the softening lengths of  $\varepsilon = 0.0074$  and  $\varepsilon = 0.0296$ , respectively, while the red line displays  $L_z$  generated by the SCF simulation.

ing them to those derived from the Gaia data, just as Antoja et al. (2018) have recently attacked this line of study.

The advantage of the present SCF code that the force field of two merging spherical galaxies is made available at each time step can be leveraged to search for the parameters that reproduce the observed tidal features of interacting disk galaxies. This line of investigation has been realized as Identikit 1 by Barnes & Hibbard (2009), and as Identikit 2 by Barnes (2011). In these programs, a simulation is carried out for two interacting self-gravitating dark halos each of which contains a galactic disk represented by test particles. If a tree algorithm is incorporated into Identikit 1 or 2, we have to carry out a simulation each time we change the configurations of the disks that are immersed in the halos, even though the configuration of the two halos remains unchanged. This is because the force field of two interacting halos cannot be found easily as long as a tree code is used. On the other hand, once an SCF simulation for two interacting halos has been carried out, even though the disk configurations are changed, we do not need to repeat such a simulation, because we have already known the time-dependent force field that the two halos created.

Another advantage that the SCF code can execute a sizable simulation in a relatively short computation time will make feasible the merging of two spherical galaxies each of which has a supermassive black hole (SMBH) at the center. For such simulations, an extremely small time step is required to cope with a wide dynamic range



originating from the existence of the SMBH. In addition, it is desirable to assign as many particles as possible to each galaxy to investigate the detailed structures down to small radii around the SMBH. These circumstances unavoidably force us to require a long computation time. Makino & Ebisuzaki (1996) and Makino (1997) conducted some pieces of pioneering work concerning the simulations mentioned above using a special-purpose computer called a GRAPE-4 system (Taiji et al. 1996) on which the NBODY1 code (Aarseth 1985) was optimized to run, and disclosed that the resulting cusps were similar to those found observationally (Lauer et al. 1995; Richstone et al. 1996). Unfortunately, because of a challenging issue at that time, they managed to assign at most hundreds of thousands of particles to a galaxy. The number of particles available to the SCF code developed here would be roughly two or three orders of magnitude larger than that they used, so that we can expect to unravel the detailed properties of the cusp formed from the above-noted merging.

## 6. CONCLUSIONS

We have developed an SCF code for merging two spherical stellar systems. This SCF code has been evaluated by comparing the results of merging simulations it generates to those obtained using a tree code for a wide range of impact parameters. We have confirmed that the results generated by the SCF code are in excellent agreement with those by a tree code: the similarity is found in the evolution of the density distribution in the merging processes, and in the density and radial and tangential velocity dispersion profiles of the merged systems.

The softening-free SCF code has revealed that the softening length of the Plummer type used in the tree code causes the advancement of the orbital phase of the two interacting systems for large impact parameters. In addition, the orbital phase becomes faster as the softening length increases. We have demonstrated that the faster advancement is caused by the larger convergence length to the pure Newtonian force.

Since the SCF code generates the force field at each time step through the expansion coefficients, we can reproduce phase space on the basis of Liouville's theorem. Furthermore, if the SCF code is incorporated into Identikit 1 or 2, the force field is known from a merging simulation, so that we can give an efficient means for finding the parameters that lead to the observed morphology of interacting disk galaxies.

The present SCF code is at least twice as fast as a tree code, so that a suitable application could be the merging of two spherical galaxies each of which contains an SMBH at the center using a sufficiently large number of particles.

We acknowledge Prof. J. E. Barnes for suggesting an application of the SCF code for merging simulations, and Prof. L. Hernquist for his careful reading of the manuscript. We are indebted to Prof. J. Makino for his valuable comments on the effects of gravitational softening. Thanks are also due to Prof. K. Takahashi for providing us with his program for constructing King models. The SCF and tree code simulations were carried out on the Cray XC30 and XC50 systems at the Center for Computational Astrophysics at the National Astronomical Observatory of Japan.

## APPENDIX

### A. THE DENSITY AND POTENTIAL BASIS FUNCTIONS

We employ the basis set constructed originally by Clutton-Brock (1973) and reformulated by Hernquist & Ostriker (1992). The density and potential basis functions, respectively, denoted by  $\rho_{nlm}(\mathbf{r})$  and  $\Phi_{nlm}(\mathbf{r})$ , are represented in polar coordinates by

$$\rho_{nlm}(\mathbf{r}) = \frac{K_{nl}}{4\pi} \frac{a^{l+5} r^l}{(a^2 + r^2)^{l+5/2}} C_n^{(l+1)}(\xi) \sqrt{4\pi} Y_{lm}(\theta, \phi), \quad (\text{A1})$$

and

$$\Phi_{nlm}(\mathbf{r}) = -\frac{a^{l+1} r^l}{(a^2 + r^2)^{l+1/2}} C_n^{(l+1)}(\xi) \sqrt{4\pi} Y_{lm}(\theta, \phi), \quad (\text{A2})$$

where  $a$  is the scale length,  $C_n^{(\alpha)}(\xi)$  are the ultraspherical, or Gegenbauer polynomials (Abramowitz & Stegun 1972) with  $\xi$  being the radial transformation written by

$$\xi = \frac{r^2 - a^2}{r^2 + a^2}, \quad (\text{A3})$$

and  $Y_{lm}(\theta, \phi)$  are the spherical harmonics that are related to associated Legendre polynomials,  $P_{lm}(\cos \theta)$ , by

$$Y_{lm}(\theta, \phi) = \sqrt{\frac{2l+1}{4\pi} \frac{(l-m)!}{(l+m)!}} P_{lm}(\cos \theta) \exp(i m \phi). \quad (\text{A4})$$

In Equation (A1), the normalization factor,  $K_{nl}$ , is expressed by

$$K_{nl} = 4n(n+2l+2) + (2l+1)(2l+3). \quad (\text{A5})$$

## REFERENCES

- Aarseth, S. J., 1985, in *Multiple Time Scales*, ed. J. U. Blackhill & B. I. Cohen (New York: Academic), 377
- Abramowitz, M., & Stegun, I. A. 1972, *Handbook of Mathematical Functions with Formulas, Graphs, and Mathematical Tables* (New York: Dover), 774
- Antoja, T., Helmi, A., Romeo-Gómez, M., et al. 2018, *Nature*, 561, 360
- Barnes, J. E., 1998, in *Galaxies: Interactions and Induced Star Formation, Dynamics of Galaxy Interactions*, ed. D. Friedli, L. Martinet, & D. Pfenniger (Berlin: Springer), 275
- Barnes, J. E. 2011, *MNRAS*, 413, 2860, *AJ*, 137, 3071
- Barnes, J. E., & Hibbard, J. E. 2009, *AJ*, 137, 3071
- Barnes, J., & Hut, P. 1986, *Nature*, 324, 446
- Clutton-Brock, M. 1972, *Ap&SS*, 16, 101
- Clutton-Brock, M. 1973, *Ap&SS*, 23, 55
- Earn, D. J. D., & Sellwood, J. A. 1995, *ApJ*, 451, 533
- Farouki, R. T., & Shapiro, S. L. 1982, *ApJ*, 259, 103
- Fukushige, T., & Makino, J. 1997, *ApJ*, 477, L9
- Hernquist, L., & Barnes, J. E. 1990, *ApJ*, 349, 562
- Hernquist, L., & Katz, N. 1989, *ApJS*, 70, 419
- Hernquist, L., & Ostriker, J. P. 1992, *ApJ*, 386, 375
- Hernquist, L., Sigurdsson, S., & Bryan, G. L. 1995, *ApJ*, 446, 717
- Howard, S., Keel, W. C., Byrd, G., & Burkey, J. 1993, *ApJ*, 417, 502
- Hozumi, S. 1997, *ApJ*, 487, 617
- Hozumi, S. 2012, *PASJ*, 64, 5
- Hozumi, S., & Hernquist, L. 1995, *ApJ*, 400, 60
- Hozumi, S., & Hernquist, L. 2005, *PASJ*, 57, 719
- Hozumi, S., Fujiwara, T., & Kan-ya, Y. 1996, *PASJ*, 48, 503
- Iwasawa, M., Tanikawa, A., Hosono, N., et al. 2016, *PASJ*, 68, 54
- King, I. R. 1966, *AJ*, 71, 64
- Lauer, T. R., Ajhar, A., Byun, Y.-I., B., et al. 1995, *AJ*, 110, 2622
- Lynds, R., & Toomre, A. 1976, *ApJ*, 209, 382
- Makino, J. 1997, *ApJ*, 478, 58
- Makino, J., & Ebisuzaki, T. 1996, *ApJ*, 465, 527
- Meiron, Y., Li, B., Holley-Bockelmann, K., & Spurzem, R. 2014, *ApJ*, 792, 98
- Miller, R. H. 1971, *Ap&SS*, 14, 73
- Miller, R. H. 1974, *ApJ*, 190, 539
- Naab, T., & Burkert, A. 2003, *ApJ*, 597, 893
- Namekata, D., Iwasawa, M., Nitadori, K., et al. 2018, *PASJ*, 70, 70
- Navarro, J. F., Frenk, C. S., & White, S. D. M. 1996, *ApJ*, 462, 563
- Navarro, J. F., Frenk, C. S., & White, S. D. M. 1997, *ApJ*, 490, 493
- Plummer, H. C. 1911, *MNRAS*, 71, 460
- Press, W. H., Flannery, B. P., Teukolsky, S. A., & Vetterling, W. T. 1986, *Numerical Recipes: The Art of Scientific Computing* (Cambridge: Cambridge University Press), 631
- Richstone, D., Gebhardt, K., Dressler, A., et al. 1996, in *IAU Symp. 174, Dynamical Evolution of Star Clusters*, ed. P. Hut & J. Makino (Dordrecht: Kluwer), 53
- Sousbie, T., & Colombi, S. 2016, *JCoPh*, 321, 644
- Taiji, M., Makino, J., Fukushige, T., Ebisuzaki, T., & Sugimoto, D. 1996, in *IAU Symp. 113, Dynamics of Star Clusters*, ed. P. Hut & J. Goodman (Dordrecht: Reidel), 373
- Tanaka, S., Yoshikawa, K., Minoshima, T., & Yoshida, N. 2017, *ApJ*, 849, 76
- Theys, J. C., & Spiegel, E. A. 1977, *ApJ*, 212, 616
- Toomre, A., & Toomre, J. 1972, *ApJ*, 178, 623
- Wallin, J. F., & Stuart, B. V. 1992, *ApJ*, 399, 29
- Weinberg, M. D., & Katz, N. 2002, *ApJ*, 580, 627
- Yoshikawa, K., Yoshida, N., & Umemura, M. 2013, *ApJ*, 762, 116